Journal of Manufacturing Processes 85 (2023) 1066–1076

Contents lists available at ScienceDirect

Journal of Manufacturing Processes

journal homepage: www.elsevier.com/locate/manpro

# Dependence of fused filament fabrication weld strength on experimental parameters: A numerical study

David A. Edwards

*Department of Mathematical Sciences, University of Delaware, Newark, DE 19716, USA*

ARTICLE INFO

*Keywords:*
Fused filament fabrication
Healing parameter
Weld strength
Fin equation
Differential algebraic equation

ABSTRACT

Objects made with fused filament fabrication (FFF) are often subject to delamination and other failures due to weak bonds between the extruded layers. Thus understanding the degree of healing of each weld is of keen interest. An unsteady fin equation model (general enough to handle any layer cross section) is proposed to track the build temperature. After being validated against experimental data, the model is used to predict the healing parameter (and hence the weld strength) for a wide range of different experimental parameters in the case of two physically realistic layer cross sections.

## 1. Introduction

In recent years, fused filament fabrication (FFF, commonly called 3-D printing) has become increasingly popular for production in many industries [1], such as electronics [2], pharmaceuticals [3], and medical and dental devices [4,5]. In this process, the desired object is composed of stacked layers, usually polymeric [6].

In order for the layers to adhere, the polymer is heated when extruded. The extruded layers have high curvature [7,8], so initially the contact area (the *weld*) between the new layer and the previously extruded layers (the *stack*) is quite small. At hotter temperatures, the polymer molecules relax more quickly, creating a bonding region that is more pliable and fluid-like. When combined with processing conditions that press the new layer onto the stack, this increases the number of entanglements formed across the layer-stack interface. Thus a hotter weld temperature causes the layers fuse together more tightly, increasing the object's strength [9–14].

To study such systems, many authors use intricate finite element or other simulations of temperature profiles throughout the stack [10,15–23]. These efforts provide detailed results, but can have drawbacks. Often times rectangular layer cross sections are used because the method can be difficult to adapt to the panoply of extrusion shapes seen in the literature [9,24–29]. Even with the use of fast solvers, the computational time will be greater than those for simpler, more idealized models. Such a differential will only accumulate if (as in this study) one needs to run the simulation multiple times in order to optimize certain experimental or process parameters.

Though more idealized models will necessarily miss some of the finer details of the system, they can still capture the essence of the FFF process, making their results surprisingly predictive. Such models have been successfully used to describe the extrusion force [30], the flow in the hot end (and hence maximal feed rates) [31–33], and the effectiveness of reheating the extruded polymer to enhance bond strength [34].

In the welding system we wish to study, Thomas and Rodríguez [35] considered a one-dimensional geometry and a single weld. They extend an isothermal result for the weld strength by solving for the temperature using a separation-of-variables approach. Edwards [36] considers multiple welds while adding the effects of radiation from the side of the stack to the one-dimensional model. By considering a quasi-steady model, the results from the separation-of-variables approach are substantially simplified.

Both of these works suffer from the drawback that they are fully one-dimensional, and hence model only stacks of rectangular layers. In this work, we present an unsteady fin model which is robust enough to handle any layer shape, while simple enough to be solved using the method of lines. We then feed the results from the heat transfer model into an expression for the *healing parameter*, which is a quantitative measurement of weld strength.

In Section 2 we present the unsteady fin model for the temperature, and introduce one model for the layer shape. In Section 3 we show how the model can be discretized using the method of lines. We illustrate that both addition of new hot layers and particular facets of the layer shape can degrade the method's convergence. In Section 4 we validate the model by comparing our temperature results to experimental data from [37] for a welded stack of ABS. In Section 5 we introduce a model for the healing parameter, which quantifies the effect of temperature on weld strength. In Section 6 we examine the effect of various design

*E-mail address:* dedwards@udel.edu.

https://doi.org/10.1016/j.jmapro.2022.11.069
Received 6 July 2022; Received in revised form 11 November 2022; Accepted 27 November 2022

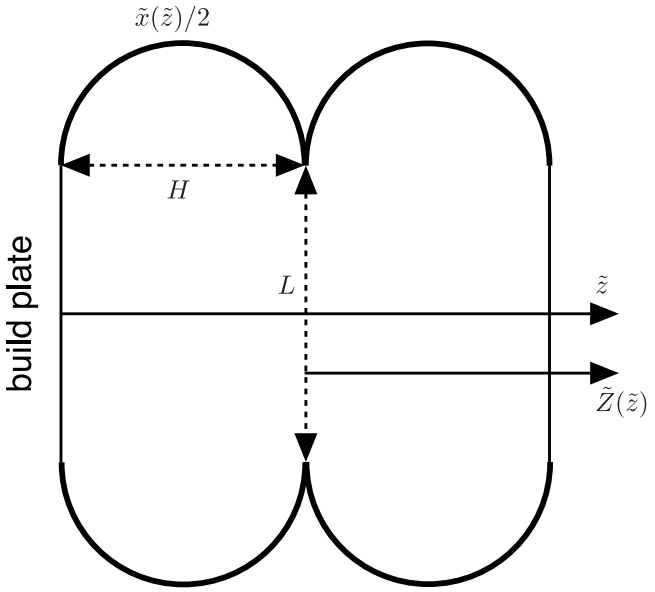


**Fig. 1.** Stack geometry, two layers (rotated 90°), illustrated with a cross section normal to the weld. Vertical lines: welds. Arcs form semicircles.

parameters on the healing parameter and consequently weld strength. In Section 7 we repeat our analysis for a different layer shape.

Our model provides results on the dependence of weld strength on various design parameters, and can do so for a wide range of layer shapes. Thus these results can help practitioners better understand the relationship between weld temperature and laminate strength, with an eye to enhancing the durability of materials fabricated using FFF.

## 2. Governing equations

To model the polymer stack, we assume a geometry shown in Fig. 1, which is rotated 90° from the experimental setup. The build plate corresponds to $\tilde{z} = 0$. The polymer emerges from the extruder with circular cross section, but then is compressed by the extruder into a shape with height $H$ and cross-sectional width $\tilde{x}(\tilde{z})$ (characteristic width $L$).

We assume that the temperature in the stack is governed by an unsteady form of the fin equation [24,36], which in this geometry is given by ([38], §9.7):

$$\rho c_p \tilde{A}(\tilde{z})\frac{\partial \tilde{T}}{\partial \tilde{t}} = k\frac{\partial}{\partial \tilde{z}}\left(\tilde{A}(\tilde{z})\frac{\partial \tilde{T}}{\partial \tilde{z}}\right) - P(\tilde{z})h(\tilde{T} - T_e), \tag{1a}$$

where $\tilde{T}$ is the temperature, $\rho$ is the density, $c_p$ is the heat capacity, $h$ is the heat transfer coefficient, $k$ is the thermal conductivity, and $T_e$ is the external temperature. This equation holds for a three-dimensional fin, so $\tilde{P}(\tilde{z})$ is the perimeter of the cross section (taken along the weld) and $A(\tilde{z})$ its area.

Each layer is assumed to have length $w$; hence taking rectangular cross sections along the weld, we have

$$\tilde{A}(\tilde{z}) = w\tilde{x}(\tilde{z}), \qquad \tilde{P}(\tilde{z}) = 2w + 2\tilde{x}(\tilde{z}), \tag{1b}$$

where $\tilde{x}(\tilde{z})$ is the width of the layer. As the length of each layer is much greater than its other dimensions, we may take the limit of large $w$ when combining Eq. (1), yielding the two-dimensional problem we will study:

$$\rho c_p \tilde{x}(\tilde{z})\frac{\partial \tilde{T}}{\partial \tilde{t}} = k\frac{\partial}{\partial \tilde{z}}\left(\tilde{x}(\tilde{z})\frac{\partial \tilde{T}}{\partial \tilde{z}}\right) - 2h(\tilde{T} - T_e). \tag{2}$$

The layers are laid down at regular time intervals spaced $t_l$ apart, where the subscript "l" refers to "layer". This process, along with the geometrical discussion above, motivates the following scalings:

$$\begin{aligned} t &= \frac{\tilde{t}}{t_l}, \qquad z = \frac{\tilde{z}}{H}, \qquad x(z) = \frac{\tilde{x}(\tilde{z})}{L}, \\ T(z,t) &= \frac{\tilde{T}(\tilde{z},\tilde{t}) - T_e}{\Delta T}, \qquad \Delta T = T_g - T_e, \end{aligned} \tag{3}$$

where $T_g$ is the glass-rubber transition temperature.

Given the layering process, the domain for the problem increases stepwise in time, as shown in Fig. 2. In particular, in dimensionless coordinates, the domain is given by

$$0 \le x \le n, \quad n-1 \le t \le n, \tag{4}$$

where $n$ is the number of layers in the stack. Thus the domain changes every time a new layer is applied.

Substituting Eq. (3) into Eq. (2), we have the following:

$$\frac{\partial T}{\partial t} = \frac{\alpha^2}{x(z)}\frac{\partial}{\partial z}\left(x(z)\frac{\partial T}{\partial z}\right) - \frac{2\alpha^2\nu}{x(z)}T, \qquad \alpha^2 = \frac{kt_l}{\rho c_p H^2}, \quad \nu = \frac{hH^2}{kL}. \tag{5}$$

Here $\alpha^2$ is the thermal diffusivity. Eq. (5) reduces to the work in [36] in the case of rectangular cross sections.

The build plate is maintained at some temperature $\tilde{T}_p > T_e$, which we scale to obtain

$$T(0,t) = T_p, \tag{6}$$

where we use the same convention as in Eq. (3) to remove the tilde on $T_p$. The exposed stack top is given by $\tilde{z} = nH$, and has surface area $\tilde{A}$. Hence we have

$$-k\tilde{A}(nH)\frac{\partial \tilde{T}}{\partial \tilde{z}}(nH,\tilde{t}) = h\tilde{A}(nH)[\tilde{T}(nH,\tilde{t}) - T_e].$$

Scaling using Eq. (3), we obtain the following:

$$\frac{\partial T}{\partial z}(n,t) = -\frac{\nu}{r}T(n,t), \qquad r = \frac{H}{L}. \tag{7}$$

Each applied layer is heated to some temperature $\tilde{T}_h$, where the subscript "h" refers to "hot". Therefore, at each integer $t = n-1$, the $n$th layer is applied and the "initial" condition for the problem resets as follows:

$$T(z,(n-1)^+) = \begin{cases} T(z,(n-1)^-), & 0 < x \le n-1, \\ T_h, & n-1 < x \le n. \end{cases} \tag{8}$$

Eq. (8) introduces a discontinuity each time a new layer is applied, which will slow numerical convergence.

As written, Eq. (5) is generic enough to handle any cross-sectional width $x(z)$, whether it arises from a specified geometrical shape [9,24–29] or is inferred from images of actual experimental data [7,37]. For the first part of the manuscript, we assume that when compressed, the layer forms a "capsule" shape consisting of a rectangle with dimensions $H$ and $L$ adjoining two semicircles of diameter $H$, as in [9,25,26] (see Fig. 1). Considering the first layer, the semicircle has radius $H/2$ and center $(H/2, L/2)$, so rewriting in terms of dimensionless coordinates, we obtain

$$x(z) = 1 + 2r\sqrt{z(1-z)}, \qquad 0 \le z \le 1, \tag{9}$$

where we have used Eqs. (3) and (7). As new layers are applied, Eq. (9) may be used if the true value of $z$ shifts to the range $[0,1]$. Therefore, we define the new variable

$$Z(z) = z - \lfloor z \rfloor. \tag{10}$$

(See Fig. 1.) Then Eq. (9) is replaced by

$$x(z) = 1 + 2r\sqrt{Z(z)[1 - Z(z)]}, \qquad 0 \le z \le n. \tag{11}$$

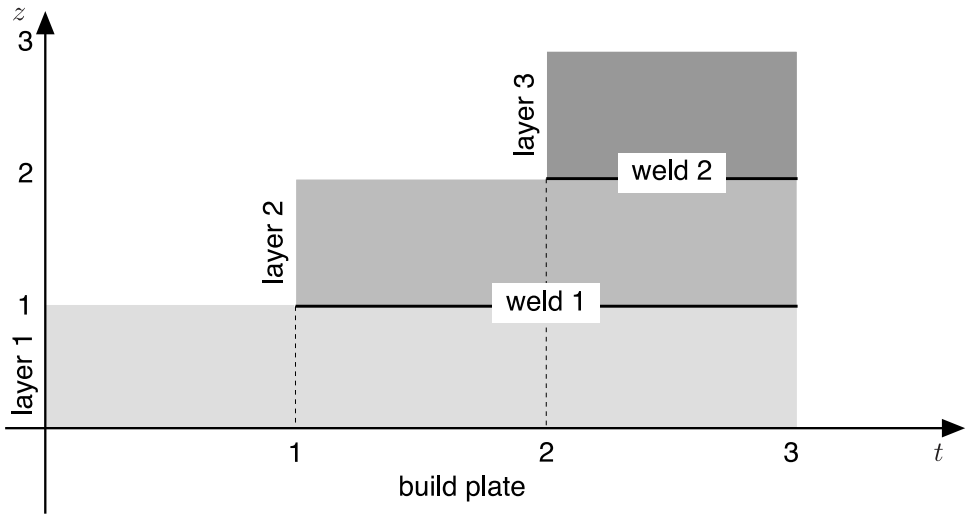


**Fig. 2.** Sequence of layers as applied (dimensionless).

## 3. Method of lines

To solve the system we use the method of lines, where the solution is discretized in $z$ only and a standard Matlab solver evolves the solution at each grid point in time. We discretize as follows:

$$z_i = \frac{i}{N}, \quad T_i(t) = T(z_i, t); \qquad 0 \le i \le nN, \tag{12}$$

where $N$ is the number of grid points per layer. Then Eq. (5) becomes

$$\frac{dT_i}{dt} = \frac{\alpha^2}{x_i}\frac{\partial}{\partial z}\left(x(z)\frac{\partial T}{\partial z}\right)\Big|_i - \frac{2\alpha^2 \nu}{x_i} T_i. \tag{13}$$

The varying coefficient in the flux creates two complications. First, conservative centered differencing must be used, yielding

$$\frac{dT_i}{dt} = \frac{\alpha^2\left\{N^2 x_{i+1/2}T_{i+1} - [N^2(x_{i+1/2}+x_{i-1/2}) + 2\nu]T_i + N^2 x_{i-1/2}T_{i-1}\right\}}{x_i},$$
$$1 \le i \le nN - 1, \tag{14}$$

where in the case that $i = 1$, the $T_0$ term can be obtained from Eq. (6):

$$T_0(t) = T_\mathrm{p}. \tag{15}$$

Second, the typical "ghost point" approach [39, §2.6.6] can no longer be used to satisfy the boundary condition Eq. (7). Instead, we replace Eq. (14) at the point $i = nN$ with a second-order noncentered difference of Eq. (7):

$$\frac{T_{nN-2} - 4T_{nN-1} + 3T_{nN}}{2N} = -\frac{\nu}{r}T_{nN}. \tag{16}$$

Since there is no time evolution in Eq. (16), the system is now in differential algebraic equation (DAE) form. There are several Matlab solvers that can handle the DAE formulation; we choose `ode23t`.

To test our algorithm, we compute the discretization error for the system using a boundary of

$$x(z) = 1 + 0.1\sin z. \tag{17}$$

Note that we use $z$ rather than $Z$, so this boundary will be perfectly smooth. We evolve the system up to $t = n + 2$, using $N = 400$ as the "exact" solution, and compare cases for $N$ with multiples of ten between 10 and 200.

The results for one layer are shown at left in Fig. 3; as expected from the discretization scheme, the error decays like $N^{-2}$. However, when we add additional layers, the error worsens, decaying only like $N^{-3/2}$ due to the discontinuity in Eq. (8) each time a new layer is applied.

In contrast to the trigonometric case in Eq. (17), Eq. (11) has a cusp at the welds, each of which are grid points by the discretization in Eq. (12). We expect the algorithm to have difficulty resolving the effects of the cusp, and this is shown in Fig. 4. Even with just one layer (shown at left), the error decays much more slowly. Because the cusp causes such difficulty for algorithm convergence, the discontinuities in Eq. (8) do not degrade the convergence much more.

## 4. Validating the model

To validate the model, we compare our weld temperature results to experimental data. For consistency between experiments with varying numbers of layers, let $W_j = T(j)$ be the temperature of the $j$th weld, numbered up from the build plate (see Fig. 2). In an experiment, the weld temperature cannot be measured directly; instead, it is inferred as the average of the midpoint temperatures of the layers above and below [37]:

$$W_j(t) = \frac{T(j-1/2, t) + T(j+1/2, t)}{2}, \quad t \ge j, \tag{18}$$

where we use the fact that the $j$th weld is formed at $t = j$.

The particular experimental data we choose is displayed in Fig. 2(a) in [37]; the author graciously provided the raw data for validation. The experimental data is for a fabricated stack of ABS one layer wide (as in Fig. 1) containing nine layers (and hence eight welds). The experimental parameters used are referenced in the Appendix of this manuscript. We fit the data for the top two welds, which we denote as $W_7$ and $W_8$ following (18) (in [37], they are denoted as $W_2$ and $W_1$).

The weld temperatures depend on three parameters: $\alpha^2$, $\nu$, and $r$. Therefore, following the successful procedure in [36], we use the Matlab `lsqcurvefit` procedure to fit our solutions to the weld data. To improve performance, in the algorithm we scale $\nu$ by a factor of 1000 to make the fit parameter roughly the same size as $r$ and $\alpha$. This ensures that the contribution of each parameter's error to the resnorm are roughly the same. Because of multiple local minima, we implemented the `GlobalSearch` procedure, which uses multiple initial guesses for the parameters to automate the search for a global minimum. We started by searching a wide range of parameters with $N = 20$. Many local minima had $r$ values that were not physically reasonable, so those were excluded. Then we ran `GlobalSearch` again with $N = 60$ for a narrower range of candidate parameter values.

The results from fitting $W_7$ and $W_8$ are shown in Fig. 5, which is generated by substituting the best parameters in a forward solver with $N = 200$. In order to compare fits on different data sets, we divide the resnorm by the number of points fit, generating the "averes" value shown. First we fit only the data from the topmost weld, then use the resulting parameters to generate curves for both welds. That

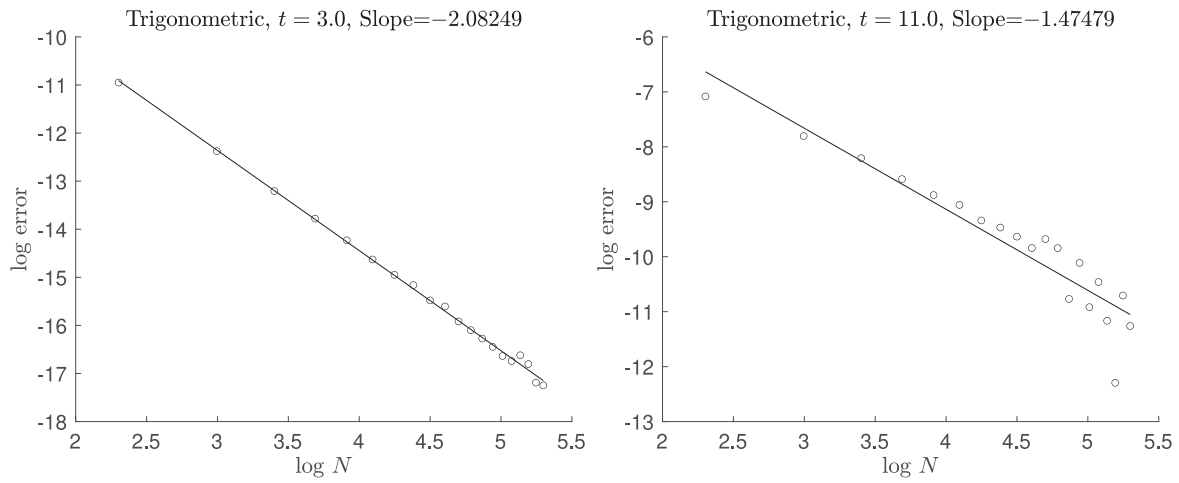


**Fig. 3.** Errors with boundary given by Eq. (17). Left: One layer. Right: Nine layers.

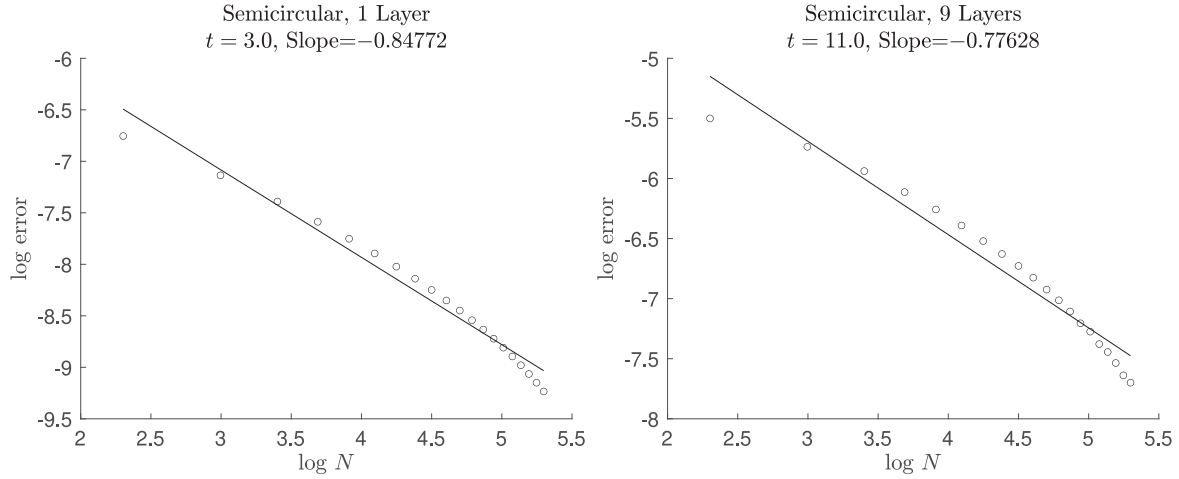


**Fig. 4.** Errors with boundary given by Eq. (11). Left: One layer. Right: Nine layers.

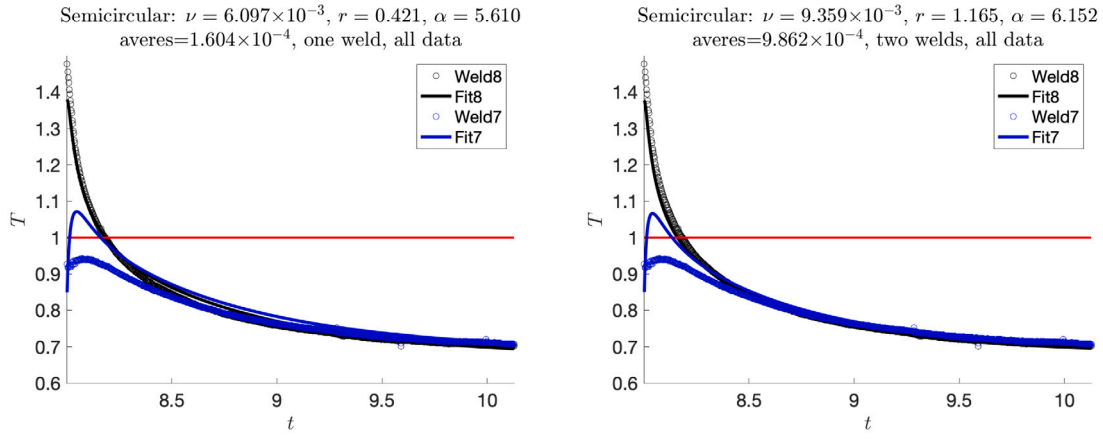


**Fig. 5.** Fit (curves) to experimental data (circles) using Eq. (11). Here the entire data set from [37] is fit; red line is $T_g$. Left: fit from using only topmost weld ("Weld8"). Right: fit from using both welds.

is shown at left. At right, we show the result by fitting the data from both welds. Note that the parameters are quite different, indicating that the solutions are somewhat insensitive to these parameters, which is consistent with multiple local minima in the optimization problem.

Unfortunately, both these fits overestimate the peak in $W_7$ when the layer is applied. One reason this could occur is that with so many data points in the exponential-like tail, accurately fitting them forces the algorithm to fit poorly those points near $t = 0$. To test this theory, in Fig. 6 we show results from fitting only the first third of the data.

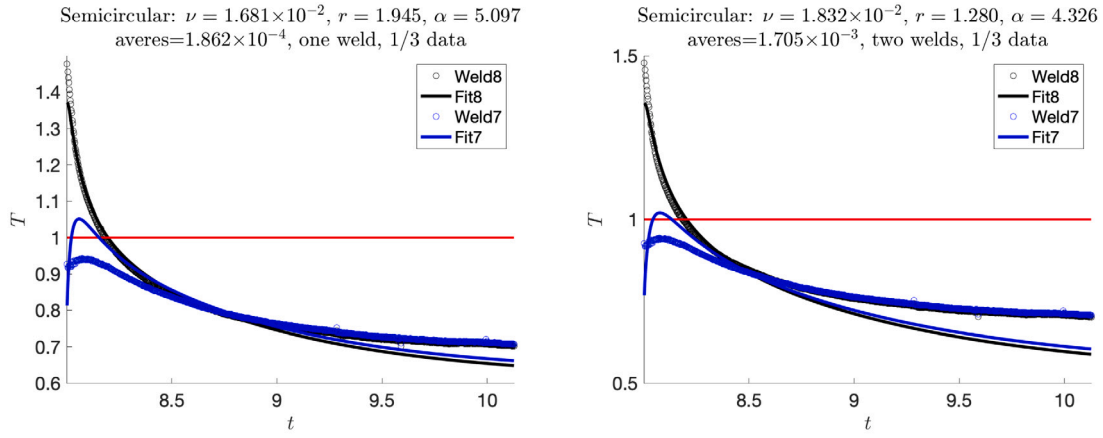


**Fig. 6.** Fit (curves) to experimental data (circles) using Eq. (11). Here only the first third of the data set from [37] is fit; red line is $T_g$. Left: fit from using only topmost weld ("Weld8"). Right: fit from using both welds.

At left, when we fit only the topmost weld, the tail matches reasonably well, but we still have a peak in $W_7$. At right, when we fit both welds, we get closer agreement to $W_7$, but at the cost of poor fit all through the exponential.

To decide which fit to use, we recall that the weld heals only when the polymer is rubbery ($T > 1$). Therefore, we want to track the weld temperature most accurately whenever it is over 1 (red line in graphs), which in this data set occurs only for the topmost weld (since the stack is so high). Thus we use the parameters at left of Fig. 5:

$$\nu = 6.097\times10^{-3}, \quad r = 0.421, \quad \alpha = 5.610, \tag{19}$$

which has the best overall fit of the topmost weld.

## 5. The healing parameter

Calculating weld temperature is important, since the strength of the weld depends on its temperature. But in order to quantify the strength of the weld, we need to model *how* the strength depends on temperature. To do so, we introduce the *degree of healing* $D$, which characterizes the strength of each weld. There are several related definitions [14,17,26,35,40–42]; we choose the following (here listed for the first weld):

$$D^2(H,\tilde{t}) = \int_0^{\tilde{t}} \frac{d\tilde{y}}{\tilde{\tau}(\tilde{T}(H,\tilde{y}))}, \tag{20}$$

where $\tilde{\tau}$ is variously referred to as the welding [14,17] or reptation [26,40,42] time.

There are two additional concepts we need to incorporate:

1. Healing occurs only when the polymer is hotter than the glass transition temperature. Hence the integrands in Eq. (20) must be multiplied by $H(\tilde{T} - T_g)$.
2. The first weld does not even exist until $\tilde{t} > t_l$ (before that, the surface $\tilde{z} = H$ is the exposed top of the stack).

Taking these two factors into account, we replace Eq. (20) with

$$D^2(H,\tilde{t}) = \int_{t_l}^{\tilde{t}} H(\tilde{T} - T_g)\frac{d\tilde{y}}{\tilde{\tau}(\tilde{T}(H,\tilde{y}))}. \tag{21}$$

Lastly we require a constitutive relationship between $\tilde{\tau}$ and $\tilde{T}$, which we obtain from Liu [43]:

$$\tilde{\tau} = \tau_0 \exp\left(\frac{3}{\tilde{T}/T_g - 0.77}\right), \tag{22a}$$

where temperatures are measured in Kelvins. Using the scalings in Eq. (3) yields

$$\tilde{\tau} = \tau_0 \exp\left(\frac{C_n}{T - C_d}\right), \qquad C_n = \frac{3T_g}{\Delta T}, \qquad C_d = \frac{0.77T_g - T_e}{\Delta T}. \tag{22b}$$

Here the subscripts "n" and "d" are for "numerator" and "denominator", respectively.

Then substituting Eqs. (3) and (22b) into Eq. (21), we obtain for any weld $j$,

$$D^2(j,t) = \frac{t_l}{\tau_0}\int_j^t H(T(j,y) - 1)\exp\left(-\frac{C_n}{T(j,y) - C_d}\right) dy, \tag{23}$$

where we have used the fact that the $j$th weld is not formed until $t = j$. Note we use the actual weld temperature, not the average given in Eq. (18) used for parameter fitting.

Note also that from Eq. (23) the degree of healing depends on the ratio $t_l/\tau_0$. Therefore, if the time between layers is much longer than the relaxation time, the layers have plenty of time to fuse, causing enhanced healing and a stronger weld. If $t_l$ is shorter than the relaxation time, there will be less time for the layers to meld, weakening the weld.

For numerical solution it is more convenient to express Eq. (23) as an ODE:

$$\frac{d(D^2)_j}{dt} = \frac{t_l}{\tau_0}H(T_{jN}(t) - 1)\exp\left(-\frac{C_n}{T_{jN}(t) - C_d}\right), \qquad t > j, \tag{24a}$$

$$(D^2)_j(j) = 0. \tag{24b}$$

The results of our simulation are shown in Fig. 7. Features of note:

1. As expected, the greatest increase in $D$ occurs when each weld is created; in other words, when the new hot layer is applied. The size of the first jump is actually largest for weld 3: because the build plate is heated to $T_g$, this weld receives heat from both directions.
2. The jump in healing occurs in a relatively narrow band after each new layer is applied because the temperature quickly descends below $T_g$ (as seen in the figures in Section 4).
3. There is at least one small jump in $D$ as additional layers above it are applied; however, our results in Section 4 indicate we should be suspicious of such jumps, as they may be an artifact of our model.
4. Since the build plate is heated to $T_g$, healing continues throughout the build for lower welds, since they receive heat from below as well as above. In particular, the lower welds have a $D$ value which is four times that of the higher welds.

## 6. Weld strength vs. experimental parameters

Stronger welds are key to the durability of items produced using FFF; hence we examine the dependence of $D$ on various experimental parameters. The results should allow engineers to design production

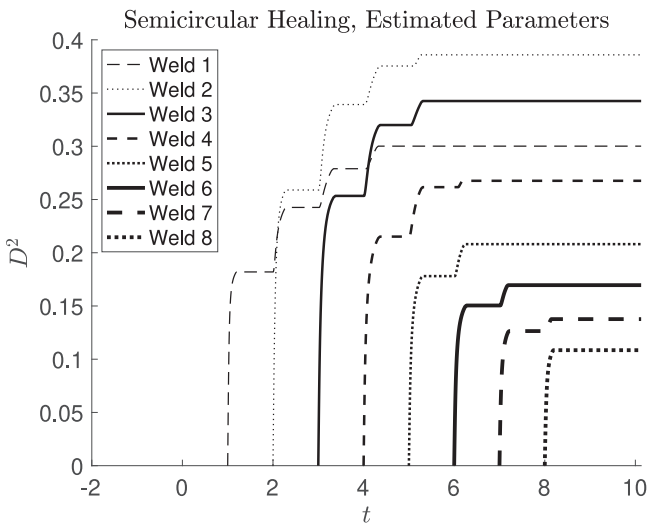


**Fig. 7.** Healing results for each weld using Eqs. (11) and (19).

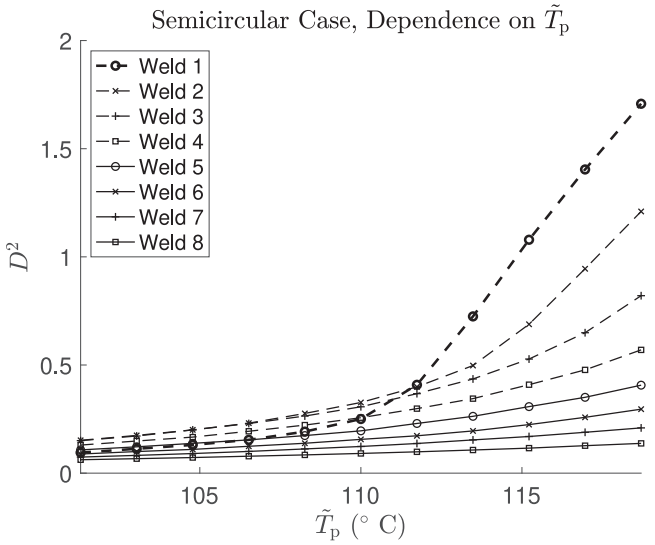


**Fig. 8.** Dependence of healing results on $\tilde{T}_p$ using Eqs. (11) and (19). Here $\tilde{T}_g = 110$°C.

processes that maximize healing. There are four parameters on which we will focus.

The first is the build plate temperature $\tilde{T}_p$. Initially, it was set to the glass transition temperature as in [37], so $T_p = 1$ (see the Appendix). At that temperature, the build will stick to the plate, which gives it extra stability [44]. Lower build temperatures may also be used, as hair spray or other adhesives can be utilized for the same purpose [45]. At the other extreme, setting the build plate temperature much higher than $T_g$ can cause the stack to warp [44]. Therefore, when examining the variance of $D$ on build plate temperature, we keep it in a narrow band: $0.9 \le T_p \le 1.1$.

The results are shown in Fig. 8 using $N = 600$ grid points. The graph clearly shows quite minimal healing when the build plate is below $\tilde{T}_g$. As the build plate gets hotter, there is additional strength in each weld, as expected. The effect is very small for high-numbered welds (which are higher in the stack and further from the build plate) and most pronounced for low-numbered welds.

In particular, consider the first weld. At low values of $\tilde{T}_p$, healing is driven by the newly applied layers, so the healing factor of the first weld is in the middle of the range. At higher values of $\tilde{T}_p$, the first

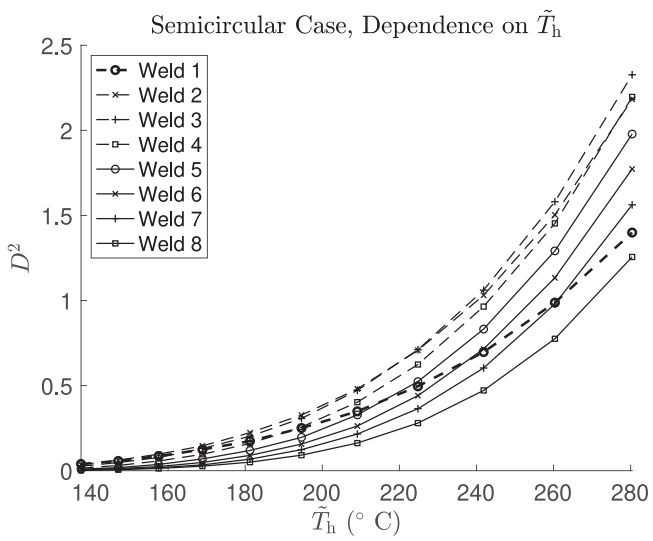


**Fig. 9.** Dependence of healing results on $\tilde{T}_h$ using Eqs. (11) and (19).

weld is kept above the glass temperature by the build plate immediately below, thus greatly increasing the healing factor.

Next we consider the effect of the heated layer temperature $\tilde{T}_h$. Though higher temperatures are correlated with higher weld strength, very high temperatures can lead to excess softening or even polymer degradation [46,47]. Therefore, when varying the heated layer temperature, we use a relatively narrow interval of $[2T_h/3, 3T_h/2]$, where $T_h$ is the temperature in the Appendix.

The results are shown in Fig. 9. As expected, increasing the temperature of the hot layer increases the healing parameter, though the effect varies depending on the position of the weld. In particular, as $\tilde{T}_h$ increases, the build plate becomes a heat sink. Hence the effect of increased layer temperature is muted for the lowest weld, which goes from having relatively high healing (compared to the other welds) to relatively low healing. A similar, more muted effect can be seen for the second weld as well.

We next examine the time between layers $t_l$, which affects the solution in two ways: through $\alpha$ (see Eq. (5)) and $D$ (see Eq. (23)). Given the typical value of $t_l$ in the Appendix, we vary $t_l$ between 5 and 10 s.

The results are shown in Fig. 10. Increasing the time between layers decreases the healing parameter slightly. This is consistent with Fig. 5, which shows that the weld is above the glass-rubber transition temperature for only a small fraction of $t_l$. The effect is slightly more pronounced for higher welds, which are more affected by the placement of new layers. Welds closer to the build plate are largely insulated and hence the temperature has already equilibrated. Therefore, the healing change in lower welds is almost nonexistent.

The final parameter we vary is $H$, which by area conservation varies the dimensions of the device:

$$HL + \frac{\pi H^2}{4} = H^2\left(\frac{1}{r} + \frac{\pi}{4}\right) = a, \tag{25}$$

where $a$ is the area of the layer with a cross section normal to the weld (as opposed to $\tilde{A}$, which is taken along the weld). The variation in $H$ can be achieved using mechanical processes [9] or noncircular orifices [27,28]. If we denote the original value of $H$ from the Appendix and the fit value of $r$ from Eq. (19) with subscript 0, we may use the fact that $a$ is constant to obtain a relationship between $r$ and $H$:

$$r = \left\{\frac{1}{H^2}\left[H_0^2\left(\frac{1}{r_0} + \frac{\pi}{4}\right)\right] - \frac{\pi}{4}\right\}^{-1}. \tag{26}$$

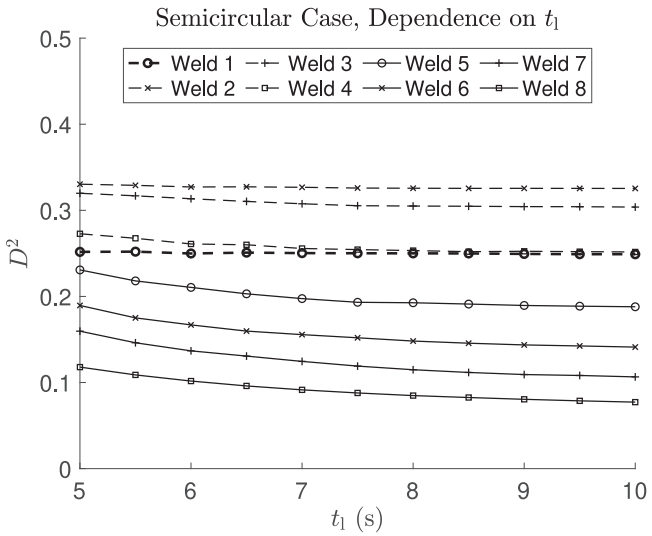


**Fig. 10.** Dependence of healing results on $t_l$ using Eqs. (11) and (19).

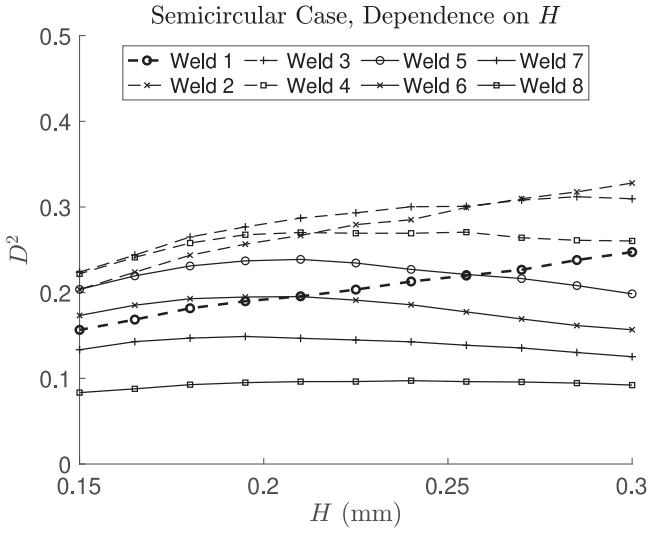


**Fig. 11.** Dependence of healing results on $H$ using Eqs. (11) and (19).

$H$ also affects $\alpha$ directly as shown in Eq. (5); if we rewrite the form for $\nu$ therein as

$$\nu = \frac{hHr}{k}, \tag{27}$$

then we can use our new $H$ and our new definition of $r$ from Eq. (26) to calculate the new value of $\nu$.

Since the extrusion diameter from the nozzle is 0.3 mm, that becomes the maximum of the tested range; the results are shown in Fig. 11. Interestingly, $D$ is not monotonic in $H$ due to the complicated interplay of the parameters listed above. Most straightforwardly, the term $\nu/r$ in Eq. (7) increases, so there is increased heat loss from the top of the stack. As $H$ increases, $\alpha$ decreases, while $\alpha^2\nu$ increases. So the balance between radiation and diffusion shifts in Eq. (5). But this shift is mitigated by the fact that as $H$ increases, $r$ increases, so the maximum value of $x$ increases by Eq. (11). Hence the increase in $\alpha^2\nu$ is balanced by an increase in $x$.

Welds in the upper part of the stack demonstrate interior maxima, as could be expected since larger $H$ corresponds to increased cooling at the exposed surface, reducing the temperatures of higher welds. Thus there is an optimum amount of pressure to exert to maximize the strength of the upper welds. The value of $H$ corresponding to an interior maximum increases with decreasing weld number. Therefore, it is possible that welds 1 and 2 have local maxima for some unphysical value of $H$ larger than 0.3 mm (though these welds are more affected by the build plate).

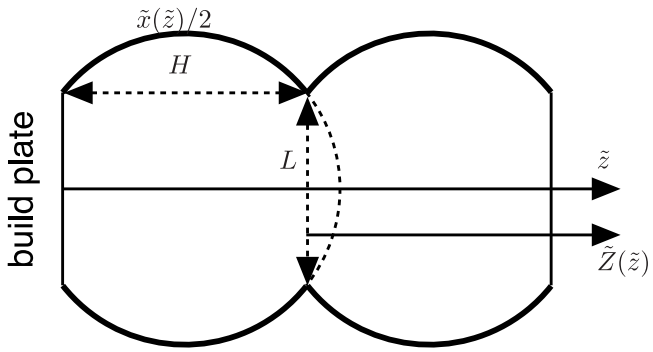


**Fig. 12.** Stack geometry, two layers (rotated 90°). Vertical lines: welds. Boundary is an arc of the illustrated circle.

## 7. A new shape

As indicated previously, the form of Eq. (5) is robust enough to handle any possible cross section. As shown in Fig. 4, the particular shape chosen in Eq. (11) has poor convergence results due to the cusp at the welds. To ameliorate this, we use a different shape motivated by the experimental photographs in Fig. 7 of [37]. In particular, we think of the layer cross section to be a circle with top and bottom lopped off (see Fig. 12).

Thus in this case the edge of the first layer is an arc of a circle with radius $\sqrt{H^2 + L^2}/2$ centered at $(H/2, 0)$; in dimensionless coordinates, we have

$$x(z) = \left[1 + 4r^2 Z(z)(1 - Z(z))\right]^{1/2}, \qquad 0 \le z \le n. \tag{28}$$

Note that though there is a jump in $x'(j)$, there is no longer a cusp.

We show convergence results in Fig. 13. With just one layer, $x'(z)$ has no singularities and we have the expected $N^{-2}$ convergence, as in the left of Fig. 3. When new layers are applied, convergence is degraded by discontinuities in Eq. (8), as well as the jump (but not singularity) in $x'(j)$. Hence the convergence rate is worse than in the smooth case shown in Fig. 3, but better than the semicircular case shown in Fig. 4.

The photograph in [37] shows a cross section which looks quite similar to Fig. 12 with $r = 1$; hence we fix that value and fit only $\nu$ and $\alpha$. The results of the parameter fitting are shown in Fig. 14, which is analogous to Figs. 5 and 6. As expected, the behavior is quite similar due to the small difference in the geometries; as before, we choose the parameters in the upper left:

$$\nu = 6.634 \times 10^{-3}, \qquad r = 1, \qquad \alpha = 5.716. \tag{29}$$

Given the similarity of the temperature traces, it is no surprise that the dependence of the healing parameter on $\tilde{T}_p$, $\tilde{T}_h$, and $t_l$ are similar, as shown in Fig. 15. To analyze the variation with $H$, we note that the area of the cross section is given by the sum of the areas of four sectors with angle $\theta$, plus the areas of the two shaded triangles shown in Fig. 16:

$$a = \frac{\theta(H^2 + L^2) + HL}{2}. \tag{30a}$$

But $\tan\theta = r$, so for the original case where $H = H_0$ and $r = 1$, we have

$$a = \frac{H_0^2}{2}\left(\frac{\pi}{2} + 1\right). \tag{30b}$$

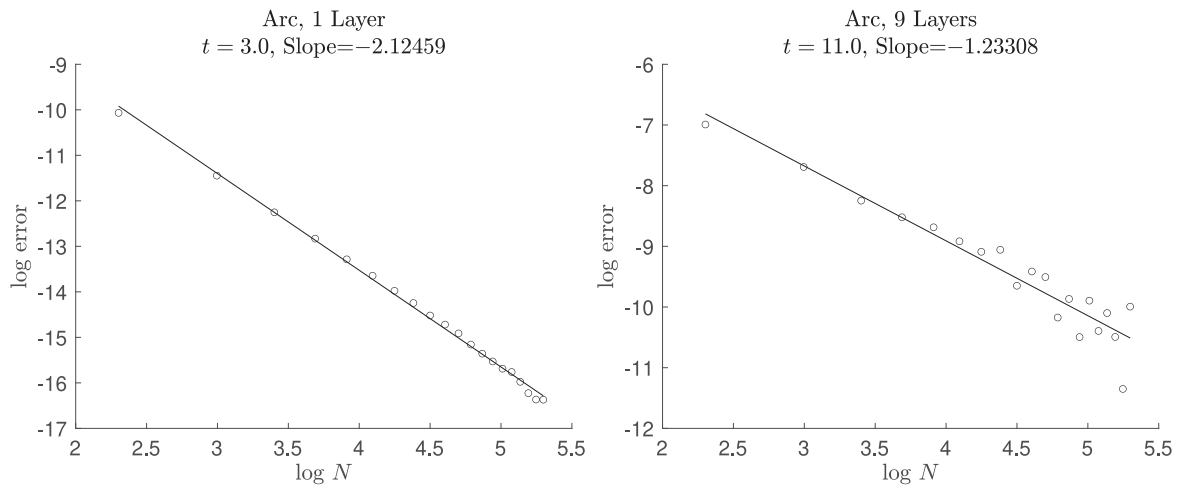


**Fig. 13.** Errors with boundary given by Eq. (28). Left: One layer. Right: Nine layers.

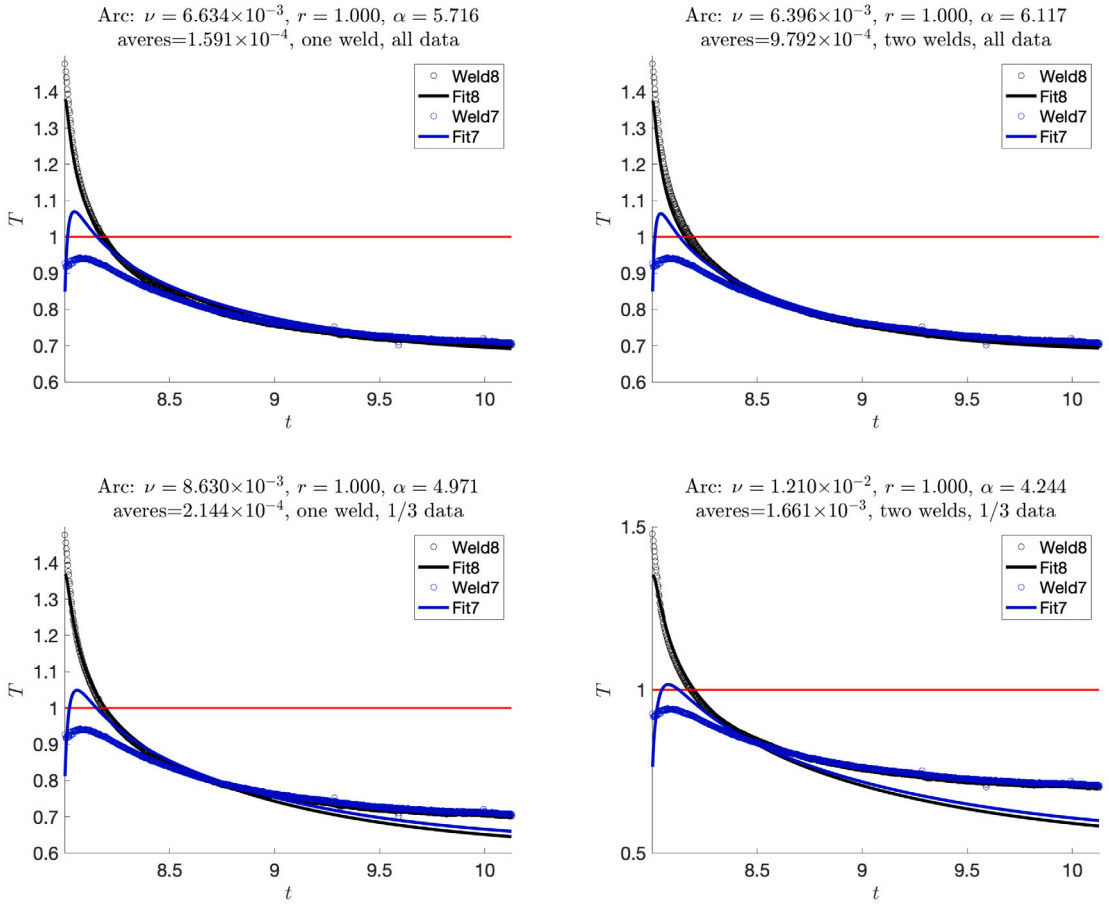


**Fig. 14.** Fit (curves) to experimental data (circles) using Eq. (28); red line is $T_g$. Top: using all data from [37]. Bottom: using first third of data from [37]. Left: fit from using only topmost weld ("Weld8"). Right: fit from using both welds.

Then combining Eq. (30), we obtain the following:

$$\tan^{-1} r\left(1+\frac{1}{r^2}\right)+\frac{1}{r}=\frac{H_0^2}{H^2}\left(\frac{\pi}{2}+1\right), \tag{31}$$

which must be solved implicitly for $r$ given some value of $H$.

The results are shown in Fig. 17, which are again quite similar in shape to Fig. 11. Since the overall results between the two models do not differ to a significant degree, the second model is more satisfying. Not only is it motivated by experiment, but also we do not have to fit as many parameters.

## 8. Conclusions and further research

In this work we studied weld strength dependence using the one-dimensional unsteady fin model in Eq. (5). To validate our model, we compared the temperature results from our simulations to the experimental data in [37] for two different choices of $x(z)$. The solution

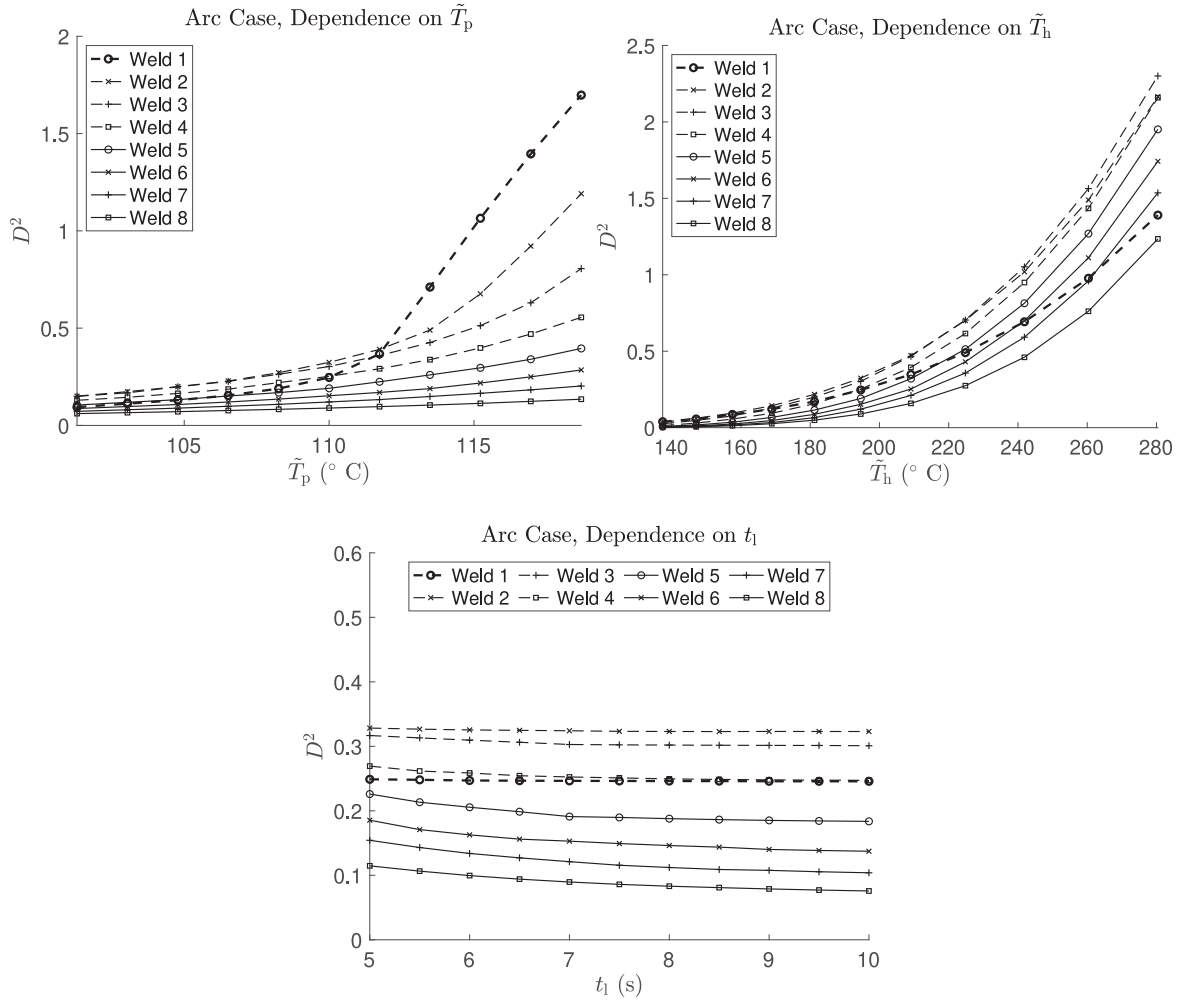


**Fig. 15.** Dependence of healing results on temperature variables and $t_l$ using Eqs. (28) and (29).

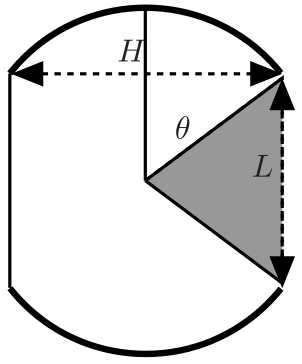


**Fig. 16.** Schematic of area calculation with the region defined by Eq. (28).

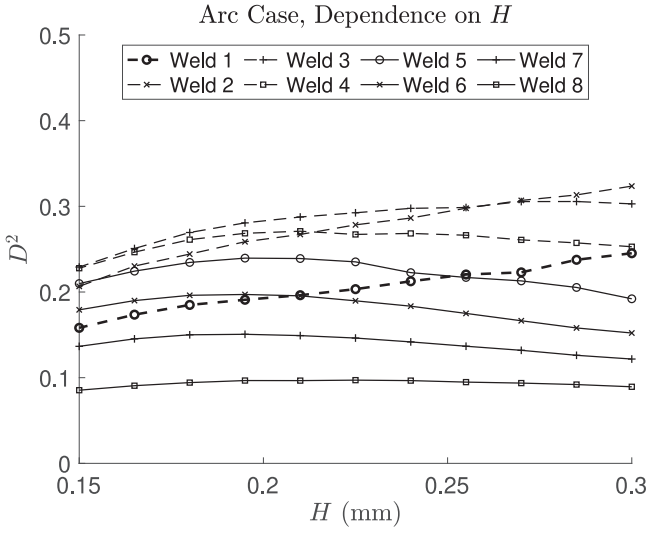


**Fig. 17.** Dependence of healing results on $H$ using Eqs. (28) and (29).

produced good results for the topmost weld, but overestimated the temperature of the weld below. We chose parameters that fit the topmost weld the best, as this was the only one in the experiment that was actively healing.

With the temperature results thus obtained, we used a constitutive relation in [43] to write Eq. (23) for the healing parameter. Our results show that the largest contribution to healing comes right after the weld's formation, with only slight additional contributions as new layers are laid down. The temperature of the build plate also contributes to healing of lower welds. The weld strengthens with increasing temperature of the newly applied layers but this effect is least pronounced for the lowest weld, whose healing is also driven by the build plate.

Since the weld temperature is above the glass-rubber transition temperature only briefly, changing the time $t_l$ between layer applications does not appreciably affect the healing parameter. The most interesting comparison is weld strength versus layer height $H$. For each weld, there seems to be a preferred height $H$ at which the healing reaches an interior maximum.

The results from this manuscript provide several promising avenues of further research. First, we can consider additional experimentally-motivated layer shapes. Second, most fabrication runs have multiple stacks aligned next to one another [17,48]. In this case, only one side of the edge stack will lose heat to the outside environment, and the interior stacks will be insulated. These phenomena can be modeled by adjusting the definition of $\tilde{P}$ in Eq. (1b).

The results in this work indicate that a well-crafted one-dimensional model can produce results that match experimental temperature data, obviating the need for more computationally intensive numerical simulations. The model is robust enough to handle many different layer shapes, and provides estimates of the healing parameter for a wide range of possible experimental parameters. Hence this model should allow practitioners to set design parameters to maximize weld strength.

## Nomenclature

Units are listed in terms of mass ($M$), length ($L$), time ($T$), and temperature ($\theta$). If a symbol appears both with and without tildes, the symbol with tildes has units, while the one without is dimensionless. Equation numbers where a variable is first defined is listed, if appropriate.

$\tilde{A}(\tilde{z})$: area of cross section along weld, units $L^2$, Eq. (1a).
$a$: area of cross section normal to weld, Eq. (25).
$C$: constants used in calculation of $D$, Eq. (22b).
$c_p$: heat capacity of polymer, units $L^2/(T^2\theta)$, Eq. (1a).
$D$: degree of healing, Eq. (20).
$h$: heat transfer coefficient, units $L/(T^3\theta)$, Eq. (2).
$H$: layer height, units $L$, Eq. (3).
$k$: thermal conductivity, units $ML/(T^3\theta)$, Eq. (1a).
$L$: layer width, units $L$, Eq. (3).
$N$: number of grid points per layer, Eq. (12).
$n$: number of layers applied, Eq. (4).
$\tilde{P}(\tilde{z})$: perimeter of cross section along weld, units $L$, Eq. (1a).
$r$: aspect ratio of layer, Eq. (7).
$\tilde{T}$: temperature, units $\theta$, Eq. (1a).
$\tilde{t}$: time, units $T$, Eq. (1a).
$W_j(t)$: estimate for temperature of $j$th weld, Eq. (18).
$w$: length of layer applied before the next height, units $L$, Eq. (1b).
$\tilde{x}(\tilde{z})$: width of the layer, units $L$, Eq. (1b).
$\tilde{y}$: dummy variable of integration, Eq. (20).
$Z(z)$: shifted value of $z$, Eq. (10).
$\tilde{z}$: height along stack, units $L$, Eq. (1a).
$\alpha$: thermal diffusivity, Eq. (5).
$\Delta T$: differential between heater and plate temperatures, units $\theta$, Eq. (3).
$\theta$: angle used in calculation of $a$, Eq. (30a).
$\nu$: dimensionless heat transfer coefficient, Eq. (5).
$\rho$: density of polymer, units $M/L^3$, Eq. (1a).
$\tilde{\tau}$: reptation time, units $T$, Eq. (20).

### Subscripts

d: indicates denominator, Eq. (22b).
e: indicates the external temperature, Eq. (1a).
g: indicates the glass transition temperature, Eq. (3).
h: indicates temperature of the applied layer, Eq. (8).
$i$: indicates grid point, Eq. (12).
$j$: indicates weld number, Eq. (18).
l: indicates the interval between layer applications, Eq. (3).
n: indicates numerator, Eq. (22b).
p: indicates temperature of the build plate, Eq. (6).
0: indicates a reference value, Eq. (22a).

**Table A.1**
Parameters from the literature.

| Parameter | Value | Reference | Parameter | Value | Reference |
|---|---|---|---|---|---|
| $c_p$ [J/(kg K)] | 1300–2100 | [7,49] | $T_g$ (°C) | 110 | [7] |
| $h$ [W/(m$^2$ K)] | 2.5–25 | [50] | $\tilde{T}_h$ (°C) | 194.6 | [37] |
| $k$ [W/(m K)] | 0.21 | [7] | $\tilde{T}_p$ (°C) | 110 | [37] |
| $H$ (mm) | 0.3 | [37] | $t_l$ (s) | 7.05 | [36] |
| $\tilde{T}_0$ (°C) | 160 | [7] | $\rho$ (kg/m$^3$) | 1030 | [7] |
| $\tilde{T}_e$ (°C) | 23 | | $\tilde{\tau}(\tilde{T}_0)$ (s) | 0.872 | [7] |

**Table A.2**
Calculated parameters.

| Parameter | Value | Parameter | Value |
|---|---|---|---|
| $C_d$ | $-1.25\times10^{-2}$ | $\alpha$ | 2.758–3.505 |
| $C_n$ | 13.2 | $\Delta T$ (°C) | 87 |
| $T_0$ | 1.57 | $\nu$ | $4.69\times10^{-3}$–$4.69\times10^{-2}$ |
| $T_h$ | 1.97 | $\tau_0$ (s) | $2.12\times10^{-4}$ |

## Declaration of competing interest

The authors declare that they have no known competing financial interests or personal relationships that could have appeared to influence the work reported in this paper.

## Acknowledgments

The author thanks Jonathan Seppala of NIST for providing the raw data for fitting. The author also thanks the reviewers for their insightful comments, which improved the final manuscript.

## Appendix

In Table A.1, we summarize the relevant parameters from the literature used in this manuscript, while in Table A.2 we calculate the parameters of interest to our model. Recall that $\tilde{T}_h$ is the temperature of the polymer when first applied. Therefore, we do not use the heater temperature of 210° C given in [37], as there is always cooling after extrusion [34,36]. Instead, we use the initial condition of the experimental data.

## References

[1] Gibson Ian, Rosen David W, Stucker Brent. Additive manufacturing technologies: Rapid prototyping to direct digital manufacturing. 1st ed. Springer Publishing Company; 2009.
[2] Kalaš David, Šíma Karel, Kadlec Petr, Polanskỳ Radek, Soukup Radek, Řeboun Jan, et al. FFF 3D printing in electronic applications: Dielectric and thermal properties of selected polymers. Polymers 2021;13(21):3702.
[3] Shaqour Bahaa, Samaro Aseel, Verleije Bart, Beyers Koen, Vervaet Chris, Cos Paul. Production of drug delivery systems using fused filament fabrication: A systematic review. Pharmaceutics 2020;12(6):517.
[4] Arslan-Yildiz Ahu, El Assal Rami, Chen Pu, Guven Sinan, Inci Fatih, Demirci Utkan. Towards artificial tissue models: Past, present, and future of 3D bioprinting. Biofabrication 2016;8(1):014103.
[5] van Noort Richard. The future of dental devices is digital. Dent Mater 2012;28(1):3–12.
[6] Steuben John, Van Bossuyt Douglas L, Turner Cameron. Design for fused filament fabrication additive manufacturing. In: Proceedings of the ASME 2015 International Design Engineering Technical Conferences and Computers and Information in Engineering Conference. International Design Engineering Technical Conferences and Computers and Information in Engineering Conference, vol. 4, 2015.
[7] Coasey Keith, Hart Kevin R, Wetzel Eric, Edwards David, Mackay Michael E. Non-isothermal welding in fused filament fabrication. Addit Manuf 2020;33:101140.

[8] Seppala Jonathan E, Migler Kalman D. Infrared thermography of welding zones produced by polymer extrusion additive manufacturing. Addit Manuf 2016;12, Part A:71–6.
[9] Luo Cheng, Mrinal Manjarik, Wang Xiang, Hong Ye. Bonding widths of deposited polymer strands in additive manufacturing. Materials 2021;14(4).
[10] Rashid Ans Al, Koç Muammer. Fused filament fabrication process: A review of numerical simulation techniques. Polymers 2021;13(20).
[11] Sun Q, Rizvi GM, Bellehumeur CT, Gu P. Effect of processing conditions on the bonding quality of FDM polymer filaments. Rapid Prototyp J 2008;14(2):72–80.
[12] Turner Brian N, Strong Robert, Gold Scott A. A review of melt extrusion additive manufacturing processes: I. process design and modeling. Rapid Prototyp J 2014;20(3):192–204.
[13] Yang F, Pitchumani R. Healing of thermoplastic polymers at an interface under nonisothermal conditions. Macromolecules 2002;35(8):3213–24.
[14] Yang F, Pitchumani R. Nonisothermal healing and interlaminar bond strength evolution during thermoplastic matrix composites processing. Polym Compos 2003;24(2):263–78.
[15] Baeza-Campuzaño Alberto, Castano Victor M. The effect of printing velocity on the temperature and viscosity of the polymer thread at the nozzle exit in 3D printers. Polimery 2021;66(2):127–38.
[16] Behdani Behrouz, Senter Matthew, Mason Leah, Leu Ming, Park Joontaek. Numerical study on the temperature-dependent viscosity effect on the strand shape in extrusion-based additive manufacturing. J Manuf Mater Process 2020;4(2).
[17] Costa SF, Duarte FM, Covas JA. Estimation of filament temperature and adhesion development in fused deposition techniques. J Mater Process Technol 2017;245:167–79.
[18] D'Amico Tone, Peterson Amy M. Bead parameterization of desktop and room-scale material extrusion additive manufacturing: How print speed and thermal properties affect heat transfer. Addit Manuf 2020;34:101239.
[19] Das Arit, McIlroy Claire, Bortner Michael J. Advances in modeling transport phenomena in material-extrusion additive manufacturing: Coupling momentum, heat, and mass transfer. Progr Addit Manuf 2021;6(1):3–17.
[20] Lotero F, Couenne F, Maschke B, Sbarbaro D. Distributed parameter bi-zone model with moving interface of an extrusion process and experimental validation. Math Comput Model Dyn Syst 2017;23(5):504–22.
[21] Mu Yue, Zhao Guoqun, Wu Xianghong, Hang Lianqiang, Chu Honghe. Continuous modeling and simulation of flow-swell-crystallization behaviors of viscoelastic polymer melts in the hollow profile extrusion process. Appl Math Model 2015;39(3-4):1352–68.
[22] Nath Paromita, Olson Joseph D, Mahadevan Sankaran, Lee Yung-Tsun Tina. Optimization of fused filament fabrication process parameters under uncertainty to maximize part geometry accuracy. Addit Manuf 2020;35.
[23] Xia Huanxiong, Lu Jiacai, Dabiri Sadegh, Tryggvason Gretar. Fully resolved numerical simulations of fused deposition modeling. Part I: Fluid flow. Rapid Prototyp J 2018;24(2):463–76.
[24] Bellehumeur Céline, Li Longmei, Sun Qian, Gu Peihua. Modeling of bond formation between polymer filaments in the fused deposition modeling process. J Manuf Process 2004;6(2):170–8.
[25] Comminal Raphaël, Serdeczny Marcin P, Pedersen David B, Spangenberg Jon. Numerical modeling of the strand deposition flow in extrusion-based additive manufacturing. Addit Manuf 2018;20:68–76.
[26] Coogan Timothy J, Kazmer David O. Prediction of interlayer strength in material extrusion additive manufacturing. Addit Manuf 2020;35:101368.
[27] Gharehpapagh Bahar, Dolen Melik, Yaman Ulas. Investigation of variable bead widths in FFF process. Procedia Manuf 2019;38:52–9.
[28] Gharehpapagh Bahar, Dilberoğlu M Uğur, Dölen Melik, Yaman Ulaş. Use of a nozzle with a rectangular orifice on a hybrid FFF system. J Addit Manuf Technol 2021;1(3):577.
[29] Gilmer Eric L, Mansfield Craig, Gardner John M, Siochi Emilie J, Baird Donald G, Bortner Michael J. Characterization and analysis of polyetherimide: Realizing practical challenges of modeling the extrusion-based additive manufacturing process. In: Seppala JE, Kotula AP, Snyder CR, editors. Polymer-Based Additive Manufacturing: Recent Developments. ACS Symposium Series, Washington: ACS Publications; 2019, p. 69–84.
[30] Percoco Gianluca, Arleo Luca, Stano Gianni, Bottiglione Francesco. Analytical model to predict the extrusion force as a function of the layer height, in extrusion based 3D printing. Addit Manuf 2021;38:101791.
[31] Edwards DA, Mackay ME, Swain ZR, Banbury CR, Phan DD. Maximal 3D printing extrusion rates. IMA J Appl Math 2019;84(5):1022–43.
[32] Luo Cheng, Wang Xiang, Migler Kalman B, Seppala Jonathan E. Upper bound of feed rates in thermoplastic material extrusion additive manufacturing. Addit Manuf 2020;32:101019.
[33] Sitison Jacob W, Edwards David A. The heat balance integral method for cylindrical extruders. J Eng Math 2020;122(1):1–16.
[34] Edwards David A, Mackay Michael E. Postextrusion heating in three-dimensional printing. J Heat Transfer 2020;142(5):052101.
[35] Thomas JP, Rodríguez JF. Modeling the fracture strength between fused-deposition extruded roads. In: 2000 International Solid Freeform Fabrication Symposium. 2000, p. 16–23.
[36] Edwards DA. Quasisteady models for weld temperatures in fused filament fabrication. IMA J Appl Math 2022;87(2):291–313.
[37] Seppala Jonathan E, Hoon Han Seung, Hillgartner Kaitlyn E, Davis Chelsea S, Migler Kalman B. Weld formation during material extrusion additive manufacturing. Soft Matter 2017;13:6761–9.
[38] Bird RB, Stewart WE, Lightfoot EN. Transport Phenomena. New York: Wiley; 1960.
[39] Langtangen HP, Linge S. Finite Difference Computing with PDEs: A Modern Software Approach. Texts in Computational Science and Engineering, Springer International Publishing; 2017.
[40] Gilmer Eric L, Anderegg David, Gardner John M, Sauti Godfrey, Siochi Emilie J, McKnight Steven H, et al. Temperature, diffusion, and stress modeling in filament extrusion additive manufacturing of polyetherimide: An examination of the influence of processing parameters and importance of modeling assumptions. Addit Manuf 2021;48:102412.
[41] Ko YS, Herrmann D, Tolar O, Elspass WJ, Brändli C. Improving the filament weld-strength of fused filament fabrication products through improved interdiffusion. Addit Manuf 2019;29.
[42] Lepoivre Arthur, Boyard Nicolas, Levy Arthur, Sobotka Vincent. Heat transfer and adhesion study for the FFF additive manufacturing process. Procedia Manuf 2020;47:948–55.
[43] Liu Chen-Yang, He Jiasong, Keunings Roland, Bailly Christian. New linearized relation for the universal viscosity-temperature behavior of polymer melts. Macromolecules 2006;39(25):8867–9.
[44] Spoerk Martin, Gonzalez-Gutierrez Joamin, Sapkota Janak, Schuschnigg Stephan, Holzer Clemens. Effect of the printing bed temperature on the adhesion of parts produced by fused filament fabrication. Plast Rubber Compos 2018;47(1):17–24.
[45] Cano Santiago, Lube Tanja, Huber Philipp, Gallego Alberto, Naranjo Juan Alfonso, Berges Cristina, et al. Influence of the infill orientation on the properties of zirconia parts produced by fused filament fabrication. Materials 2020;13(14).
[46] Harris Muhammad, Potgieter Johan, Ray Sudip, Archer Richard, Arif Khalid Mahmood. Preparation and characterization of thermally stable ABS/HDPE blend for fused filament fabrication. Mater Manuf Process 2020;35(2):230–40.
[47] Shaqour Bahaa, Abuabiah Mohammad, Abdel-Fattah Salameh, Juaidi Adel, Abdallah Ramez, Abuzaina Waleed, et al. Gaining a better understanding of the extrusion process in fused filament fabrication 3D printing: a review. Int J Adv Manuf Technol 2021;114(5):1279–91.
[48] Zhou M, Zhou X, Si L, Chen P, Li M, Zhang Y, et al. Modeling of bonding strength for Fused Filament Fabrication considering bonding interface evolution and molecular diffusion. J Manuf Process 2021;68:1485–94.
[49] Lechner Manfred Dieter. Polymers. In: Warlimont Hans, Martienssen Werner, editors. Springer Handbook of Materials Data. Springer International Publishing; 2018, p. 489–540.
[50] Kosky Philip, Balmer Robert, Keat William, Wise George. Exploring Engineering. 5th ed. Academic Press; 2021.